

A Quasiparticle Detector for Imaging Quantum Turbulence in Superfluid $^3\text{He-B}$

S. L. Ahlstrom · D. I. Bradley · S. N. Fisher · A. M. Guénault · E. A. Guise · R. P. Haley · S. Holt · O. Kolosov · P. V. E. McClintock · G. R. Pickett · M. Poole · R. Schanen · V. Tsepelin · A. J. Woods

Received: 2 December 2013 / Accepted: 20 February 2014

© The Author(s) 2014. This article is published with open access at Springerlink.com

Abstract We describe the development of a two-dimensional quasiparticle detector for use in visualising quantum turbulence in superfluid $^3\text{He-B}$ at ultra-low temperatures. The detector consists of a 5×5 matrix of pixels, each a 1 mm diameter hole in a copper block containing a miniature quartz tuning fork. The damping on each fork provides a measure of the local quasiparticle flux. The detector is illuminated by a beam of ballistic quasiparticles generated from a nearby black-body radiator. A comparison of the damping on the different forks provides a measure of the cross-sectional profile of the beam. Further, we generate a tangle of vortices (quantum turbulence) in the path of the beam using a vibrating wire resonator. The vortices cast a shadow onto the face of the detector due to the Andreev reflection of quasiparticles in the beam. This allows us to image the vortices and to investigate their dynamics. Here we give details of the design and construction of the detector and show some preliminary results for one row of pixels which demonstrates its successful application to measuring quasiparticle beams and quantum turbulence.

Keywords Quantum turbulence · Superfluid $^3\text{He-B}$ · Andreev reflection · Ballistic quasiparticles · Tuning fork array · Quasiparticle camera

1 Introduction

Quartz tuning forks are commercially available and commonly used as a frequency standard for timing devices such as watches. In recent years, they have become a

S. L. Ahlstrom · D. I. Bradley · S. N. Fisher (✉) · A. M. Guénault · E. A. Guise · R. P. Haley · S. Holt · O. Kolosov · P. V. E. McClintock · G. R. Pickett · M. Poole · R. Schanen · V. Tsepelin · A. J. Woods
Department of Physics, Lancaster University, Lancaster LA1 4YB, UK
e-mail: s.fisher@lancaster.ac.uk

popular tool in quantum fluids [1] and solids [2] research. The response of a fork can be easily calibrated to measure the prong velocity [3,4]. Quartz tuning forks have very high quality factors, of order 10^5 , making them sufficiently sensitive to study the mechanical properties of helium fluids at low temperatures. They have found many applications in superfluids research including measurements of viscosity [5–7], quantum turbulence in ^4He [8–10], cavitation [11], Andreev scattering in $^3\text{He-B}$ [12,13] and acoustic modes [14–16]. Here we describe their use as sensitive probes of ballistic quasiparticles in superfluid $^3\text{He-B}$. We use arrays of forks to form a rudimentary quasiparticle camera to measure the cross-sectional profile of a beam and how it evolves with time. The device can be used to image superfluid ‘structures’ which scatter ballistic excitations, such as vortices and quantum turbulence.

Visualisation techniques are well established to study turbulence in classical fluids [17]. Typically, tracer particles are injected into the fluid which are tracked along illuminated planes in the flow. The particles are sufficiently small to accurately follow the fluid flow. The visualisation of turbulence in a superfluid is far more demanding due to the very low temperatures required and the inviscid nature of the superfluid component.

There have been a number of developments in recent years to visualise turbulence in superfluid ^4He . At relatively high temperatures hydrogen particles have been used as tracers to visualise the flow [18–20]. Understanding the motion of the hydrogen particles is a complex problem since they are influenced by the competing effects of normal fluid flow and quantised vortices in the superfluid component [21]. Flow of the normal fluid has also been visualised using He excimer molecules [22]. In the low temperature limit quantum turbulence has been investigated with ion trapping techniques [23] and it has recently been shown that excimers have a significant trapping diameter for binding to vortex cores at low temperatures [24]. This provides possibilities for visualising quantum turbulence at low temperatures using excimer molecules.

The study of quantum turbulence in superfluid ^3He requires sub-mK temperatures [25]. At such low temperatures it is extremely difficult to inject any kind of impurity tracer particles or to make optical measurements to track them. However, quasiparticle excitations make ideal probes of superfluid flow in $^3\text{He-B}$ at very low temperatures. Motion of a superfluid with velocity \mathbf{v} tilts the excitation dispersion curve according to the Galilean transformation which shifts the energies by $\mathbf{p} \cdot \mathbf{v}$ [26]. The shift thus acts as an energy barrier for incident excitations with momenta along the flow direction. The thermal excitations in $^3\text{He-B}$ have very low energies and high momenta. Consequently, the energy barrier due to flow is relatively large. Excitations with insufficient energy are Andreev reflected by the flow: quasiparticles become quasiholes and vice versa [26, 27]. Andreev reflection gives almost perfect retroreflection with very little momentum transfer, thus providing an ideal passive probe of the flow [28].

Andreev reflection from superfluid flow has been measured directly [29] at very low temperatures using quasiparticle beam and black-body radiator techniques. The measurements are made at very low temperatures where the excitations are ballistic so the excitations only undergo normal scattering with the container walls. A black-body [30] radiator is a box containing two vibrating wire resonators, one used as a heater and the other as a thermometer [31]. A small orifice provides a weak thermal link to the surrounding superfluid. The box is heated, producing a thermal distribution

of quasiparticle excitations which is measured with the thermometer wire. The heat leaves the radiator as a beam of ballistic quasiparticles. If some excitations in the beam undergo Andreev scattering, then they accurately retrace their path back into the radiator causing a rise in the temperature (excitation density) within the radiator. This technique has been used to directly measure Andreev reflection from the flow generated by a vortex lattice [32] and by quantum turbulence [33,34]. The radiator also provides very sensitive calorimetry which has been used to study the decay of quantum turbulence [35].

In the current experiment we use a radiator to generate a quasiparticle beam to ‘illuminate’ a detector. Owing to Andreev reflection, vortices illuminated by the beam cast a shadow. The vortices are generated by a vibrating wire resonator [36]. Here we focus on the design and development of the detector to measure the quasiparticle shadows. The detector comprises 25 custom-made miniature tuning forks individually housed in cylindrical channels in a copper matrix. The damping experienced by each fork provides a measure of the local incident quasiparticle flux, thus allowing us to ‘image’ the quasiparticle beam and to construct a shadowgraph of vortices in the path of the beam. The spatial resolution is limited but it should be sufficient to gain useful information on the spatial profile of vortices generated by the wire as well as their dynamics. Based on calculations of Andreev reflection [37], we believe that the detector should be capable of detecting a single vortex line.

2 The Tuning Fork Arrays

The tuning forks were custom-manufactured on wafers provided by Statek Corporation; an example is shown in Fig. 1. A number of identical wafers were made with two different thicknesses which determines the prong width, $W = 75 \mu\text{m}$ and $W = 50 \mu\text{m}$. All of the tuning forks have a common thickness of $T = 90 \mu\text{m}$ and the spacing between the prongs is $D = 90 \mu\text{m}$. The prong lengths L vary to give different resonant frequencies. The wafer holds eight tuning fork arrays designed specifically for the quasiparticle detector. Each array has five forks with different lengths. The centres of the forks are 1.1 mm apart. The prong lengths are chosen to give well-separated resonant frequencies to avoid inter-fork coupling: the forks become strongly coupled when their resonances overlap, so it is important to ensure that the fundamental resonant frequencies f_0 are well-separated compared to the frequency width Δf_2 of each resonance. The eight detector arrays have forks with resonant frequencies in the range of 20–40 kHz. In each array the resonant frequencies are designed to be approximately equally spaced and span the frequency range. The lengths of the prongs are slightly offset for each array. This results in equally-spaced resonant frequencies for the 40 forks in the eight arrays spanning the range 20–40 kHz, and the largest possible separation of frequencies for forks on the same array to avoid cross-coupling.

The wafer also holds other forks which have been used for different experiments in superfluid ^4He . There are several single forks which have fundamental resonant frequencies in the range 6–32 kHz and an additional array with forks having resonant frequencies in the range 20–160 kHz. These were used to study frequency dependent properties in superfluid ^4He such as sound emission [15] and turbulent drag [4].

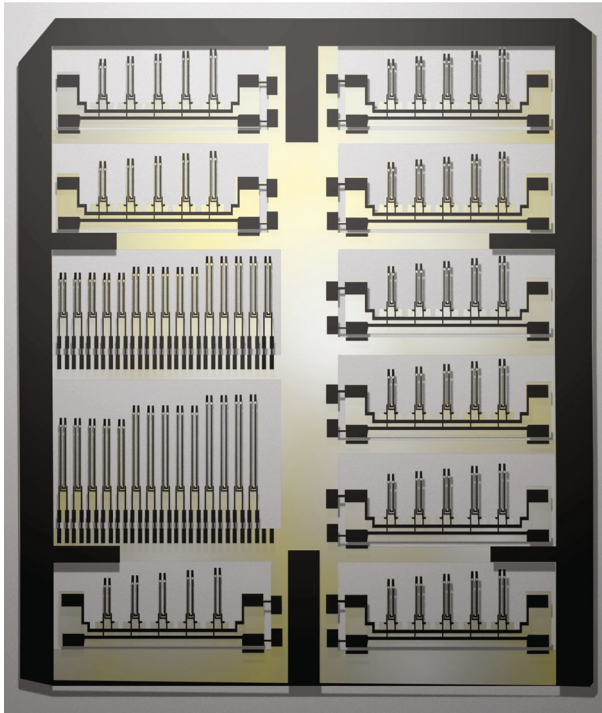


Fig. 1 Photograph (enhanced) of a single wafer holding several single forks and fork arrays. The arrays on the *right* and *upper left* sides of the wafer were designed for the quasiparticle detector. The *two banks* of single forks, *centre left*, and the *bottom left* fork array were used for other experiments. The dimensions of the wafer are approximately 25.5×22.5 mm (Color figure online)

Each array is attached to the frame of the wafer by two small tabs at one end next to the contact pads. The single forks are connected by a single tab. The arrays are removed from the wafer by carefully applying a small force to the contact pad area.

The forks in each array are driven and measured in parallel, as described below, so they share a common pair of leads. Each array has a pair of contact pads at each end but connections only need be made to one of these. In practice connections to external leads were usually made at the same end of the array.

To connect the external leads to the contact pads, the opposite end of the array is held in a pair of lightly-clamped tweezers. For the $75 \mu\text{m}$ arrays, fine stainless steel tweezers were used with heat shrink to soften the tips. This technique was not suitable for the $50 \mu\text{m}$ arrays since these were far more fragile. For these we used a clamp made from two pieces of Stycast impregnated paper, held together by stainless steel tweezers. The external leads were $100 \mu\text{m}$ diameter copper clad single core NbTi wire. Each lead was positioned with a micromanipulator. When tinning and soldering the wires to the contact pads, care was needed to ensure the pads were not destroyed by overheating. An example of a single array with lead connections is shown in Fig. 2.

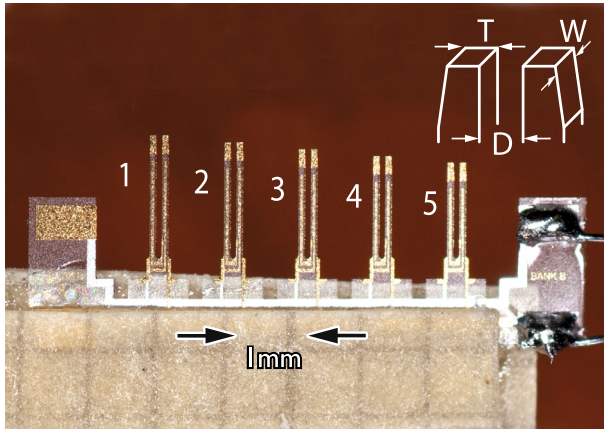


Fig. 2 Photograph of a single fork array with five forks of varying lengths. The base of the array is sandwiched between *two pieces* of Stycast-impregnated paper to give a rigid support for testing. Leads are attached to the *righthand contact pads* (Color figure online)

3 Measurement Setup

The tuning forks are driven at or around their fundamental resonant frequencies by a voltage V supplied by a waveform generator with suitable attenuators. The driving force on each prong is given by

$$F = \frac{aV}{2} \tag{1}$$

where a is the fork constant. The resulting prong motion generates a current I which is measured with a custom-made current-to-voltage converter [38] and a 2-phase lock-in amplifier referenced to the generator. The velocity of the prong tips v is given by

$$v = \frac{I}{a} \tag{2}$$

The fork constant is given by [6]

$$a = \sqrt{\frac{4\pi m_{\text{eff}} \Delta f_2 I_r}{V_r}} \tag{3}$$

where I_r and V_r are the current and voltage amplitudes at the resonant frequency, Δf_2 is the frequency width of the resonance and the effective mass can be assumed to be equal to one quarter of the prong mass [15] $m_{\text{eff}} = \rho L T W / 4$ where ρ is the density of quartz. Direct optical measurements of the fork motion [3,4] show that the fork constant given by Eq. 3 is usually accurate to better than 10 %.

The five forks in each array are measured simultaneously using the setup shown in Fig. 3. Each fork is driven with a separate generator and measured with a separate lock-in amplifier. The drive voltages from the five generators for each array are combined with a custom-made summing amplifier unit with active attenuation and fed into the

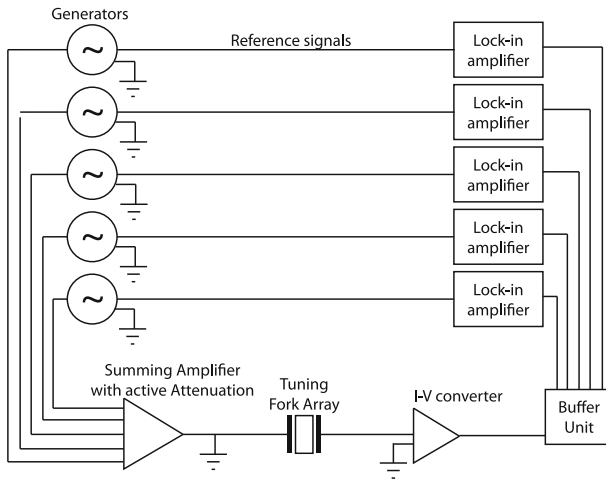


Fig. 3 Schematic of the measurement setup for a tuning fork array. Each fork is driven and measured independently with its own generator and lockin amplifier, but the forks use a common pair of leads and a common I–V converter, see text

single input lead of the array. The single output lead is fed to a custom-made I–V converter [38]. The output of the I–V converter is split by a custom-made buffer unit and fed to the five lock-in amplifiers. Each lock-in amplifier is referenced to the corresponding generator.

This set-up is very versatile, allowing us to measure each fork independently and simultaneously with other forks on the same array.

4 Initial Tests and Characterisation of the Arrays

Initial measurements on the arrays were made in air at room temperature. For each fork, the amplitude of the driving voltage was held at a relatively low level whilst the frequency was swept through the fundamental resonance. Each resonance was fitted to the ideal Lorentzian lineshape [4, 15] to obtain the resonant frequency f_0 , the frequency width Δf_2 and the resonant signal from which we could infer the fork constant using Eq. 3. The frequency width is proportional to the damping force per unit velocity [4, 15].

The first measurements showed that some of the forks had a significantly higher intrinsic damping than other forks. The extra damping depended on the location of the fork and on how the array was held. We attributed this to flexing of the base of the array. The extra damping was eliminated by securing the array to a rigid base. Consequently all future arrays were securely fixed to a solid base for testing. We found that it was sufficient to clamp the arrays between two thin sheets of Stycast-impregnated graph paper as shown in Fig. 2.

The resonant frequency of each fork could be quite accurately predicted from the ideal cantilever model which predicts [4, 15]:

$$f_0 = \frac{1}{2\pi} \sqrt{\frac{ET^2}{12\rho}} b_0^2 \quad (4)$$

where $E = 7.87 \times 10^{10} \text{ Nm}^{-2}$ is the Young's modulus of quartz and the wavenumber of the fundamental mode is $b_0 = 1.875 / L$. We have tested forks from several nominally identical wafers. The frequencies of the forks on different wafers are usually quite close, but occasionally they are found to differ significantly, up to a few hundred Hertz. In this case, it was found that all of the forks on the wafer were shifted by approximately the same factor so the differences can be attributed to small variations in the manufacturing conditions for each wafer.

The ultimate sensitivity of the tuning forks to quasiparticles in superfluid $^3\text{He-B}$ at very low temperatures is limited by the intrinsic damping of the forks, so it is important to ensure that this is sufficiently small for each of the forks in the detector. For this purpose, we measured many fork arrays in vacuum at 4.2 K using a small test rig that can be placed in a liquid ^4He transport dewar. Numerous arrays were tested from different wafers. All of the forks were found to have intrinsic widths of around $\Delta f_2 \sim 100$ mHz, corresponding to a quality factor $Q = f_0/\Delta f_2$ which exceeds 10^5 .

Further measurements with the single tuning forks and with the arrays with a higher range of frequencies were made in normal and in superfluid ^4He to study the crossover from hydrodynamic to acoustic drag [15]. Here it was found that the damping becomes dominated by acoustic emission at frequencies larger than ~ 100 kHz. The tuning forks used for the detector have resonant frequencies well below this so acoustic damping is entirely negligible in this case.

5 Detector Design and Construction

It was originally planned to use four of the arrays to build a $4 \times 5 = 20$ pixel detector. However, since the forks were well behaved with low intrinsic damping and resonant frequencies close to the design values, there was no danger of the fork resonances overlapping so we decided to make a slightly larger 25 pixel detector. This enables better resolution with a central pixel surrounded by a symmetric number of adjacent pixels which can be aligned with the quasiparticle beam.

The body of the detector was made from a copper block, see Fig. 4. A number of prototypes were constructed to find the best design for holding the arrays rigidly and for ease of construction. The final block had dimensions $5.7 \times 5.7 \times 4.0$ mm. To form the pixel cavities, 25 holes were drilled through the block, each 1.0 mm in diameter. The holes form a square lattice with spacing of 1.1 mm so the wall thickness between adjacent holes is just 0.1 mm at its thinnest point. On the rear of the block are five 0.1 mm wide and 1 mm deep channels passing through the centre of each row of holes. This provides a slot to seat each array. Each array is shaped with slots either side of each fork, shown in Fig. 2, to interlock with the copper walls separating adjacent pixels. This provides good rigidity and good alignment of the forks with the centres of the pixels, see Fig. 4a.

Our initial tests showed that the $50 \mu\text{m}$ and $75 \mu\text{m}$ arrays had similar intrinsic frequency widths in vacuum at 4.2 K. We therefore decided to use the $50 \mu\text{m}$ arrays

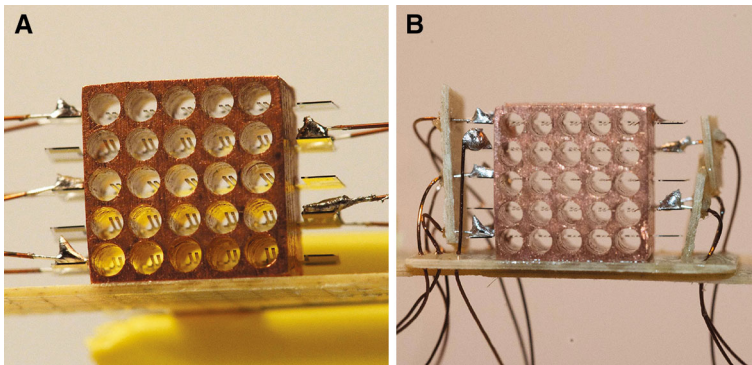


Fig. 4 **a** Photograph of the detector with the arrays installed. The external leads are attached on alternate sides. The tuning forks are seen to be approximately in the centres of each hole. Each hole with tuning fork forms a single pixel of the 25 pixel detector. **b** Photograph of the detector showing the supports for the leads which now pass through the Stycast-impregnated paper baseplate (Color figure online)

since these will provide better sensitivity to quasiparticles (the frequency width due to thermal damping from ballistic quasiparticles is higher for smaller, lighter objects [26, 39]). The five arrays chosen for the detector had forks with resonant frequencies spaced by a minimum of 250 Hz. The frequency widths of the fork resonances in air are approximately 10 Hz so the fork frequencies were sufficiently well spaced to prevent cross-coupling even in air at room temperature. This was convenient for testing the detector before installation.

The base of the copper block was first glued to a Stycast-impregnated paper baseplate. Each of the arrays was carefully inserted into the copper block using a micromanipulator. The base of the array slotted into the appropriate 100 μm channel in the back of the block. The array was then released from the micromanipulator and tweezers were used to nudge the array into its final position, with the base of the array sitting flush with the rear face of the copper block. Finally, a very small amount of thick (partly cured) Stycast-1266 was applied to the outer slot at the edge of the copper block on either side and left to cure fully. The process was repeated for each array. Two of the arrays broke after being glued in place but fortunately we were able to replace these without disturbing the other arrays. The arrays were mounted with external leads on alternate sides of the block. A photograph of the detector completed to this stage is shown in Fig. 4a.

Before the detector could be mounted in the experimental cell, the leads needed to be bent down to come through the Stycast-impregnated paper base. This was not trivial since bending the wires at this stage would put sufficient force on the ends of the arrays to snap them. Therefore two side-panels were made from Stycast-impregnated paper to hold the wires securely close to the contact pads. The holes in each side-panel were large enough to comfortably slide the wires through, before gluing the panel in place on the detector base. Unfortunately, one of the contacts on the upper array broke during this procedure so a new connection had to be made to one of the contacts on the other side of the array. The completed detector with lead supports is shown in Fig. 4b.

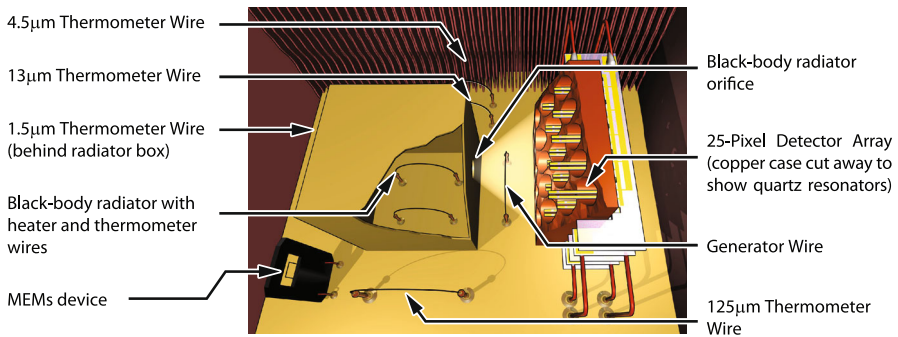


Fig. 5 Schematic of the experimental volume surrounded by the refrigerant sinter stack. The radiator is designed to illuminate the detector with a beam of quasiparticles centred on the central pixel. A vibrating wire in the path of the beam is used to generate vortices which cast a quasiparticle shadow on the detector. The generator wire is approximately equidistant between the wall with the radiator orifice and the front face of the detector which are approximately 2 mm apart. The cell has various thermometers and a MEMS device not used for the measurements described here (Color figure online)

Finally the detector was mounted in a Lancaster style nuclear cooling stage [40,41] with the Stycast paper base forming part of the inner cell wall. The experimental volume shown in Fig. 5 is roughly rectangular in shape and is cut out of the inner cell refrigerant stack, ~ 80 thin copper sheets coated with silver sinter [40,41]. The refrigerant stack thus forms the vertical sides and the upper horizontal sides of the experimental volume. This configuration optimises the thermal coupling between the refrigerant and the superfluid in the experimental volume. This is crucial for performing quasiparticle beam experiments at very low temperatures.

The experimental volume also contains a black-body radiator with its orifice aligned approximately with the centre of the detector array, a ‘generator’ vibrating wire for producing quantum turbulence, and four thermometer vibrating wires of varying wire diameters to measure different temperature ranges. There is also a MEMS device which was not used for the experiments described here, but is shown for completeness. The top of the generator wire loop was positioned to be approximately in line with the black-body radiator orifice and the central pixel of the detector.

6 Preliminary Measurements

Preliminary measurements were made with just the central array. The five forks in the array are driven continuously at their respective resonance frequencies, whilst we monitor the resulting signals. At resonance the damping force is balanced by the driving force and the velocity is maximised and in-phase with the driving force. In practice we measure the in-phase and out-of-phase (quadrature) components of the signals with respect to the driving force. An automated program is used to maintain resonance by adjusting the drive frequency to ensure that the ratio of the quadrature and in-phase signals is kept below some small value, typically 1 %. This allows us to infer the width of the resonance Δf_2 for each tuning fork which provides a measure of the damping. The program also adjusts the drive to maintain the velocity at some

specified value. The velocity is always chosen to be below the critical velocity for pair-breaking [42] so the damping has contributions only from thermal quasiparticles and from intrinsic losses.

The total damping on the forks is the sum of the quasiparticle damping and the intrinsic damping, $\Delta f_2 = \Delta f_2^{QP} + \Delta f_2^i$. The intrinsic damping is measured at the lowest temperatures where the thermal quasiparticle damping is entirely negligible. At low velocities, the drag force from thermal quasiparticles is proportional to the velocity [26]. In this case the corresponding damping Δf_2^{QP} is velocity independent and provides a measure of the local density of quasiparticles. To improve the signal-to-noise ratio, the forks are driven to a higher velocity, $\sim 5 \text{ mm s}^{-1}$, where the drag becomes non-linear. The non-linear drag is however well understood [27,39] and is easy to characterise [13] to infer the low velocity damping Δf_2^{QP} . The power dissipated by the tuning forks is very small, much less than 1 pW, and has negligible effect on the measurement.

To a first approximation, each pixel can be considered to be a miniature blackbody radiator. In this case, the density of quasiparticles within each pixel is approximately proportional to the flux of incident quasiparticles. Hence the quasiparticle damping Δf_2^{QP} of the forks can be used to measure the local beam intensity.

Figure 6 shows measurements of the central array of forks whilst the black-body radiator is heated to give a beam power of $\dot{Q} = 23.5 \text{ pW}$. We show the quasiparticle damping $\Delta f_{2,p}^{QP}$ for each of the central row of pixels, labelled $p = 1$ to $p = 5$. The x -axis shows the distance from the central pixel. The experiment was designed to have the beam centred on the centre pixel. In practice however it was very difficult to align the detector precisely. The data in Fig. 6 indicate that the beam was actually centred between pixels $p = 2$ and $p = 3$.

The quasiparticle damping on the forks also has a contribution from the background quasiparticles governed by the temperature of the cell, Δf_2^T . In practice this rises due to

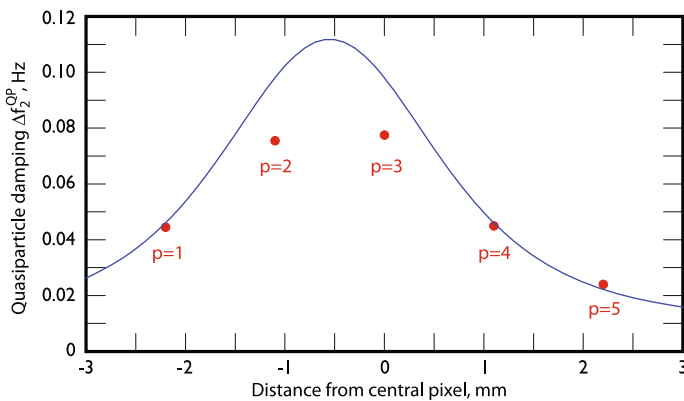


Fig. 6 The quasiparticle damping $\Delta f_{2,p}^{QP}$ for each of the central row of pixels, labelled $p = 1$ to $p = 5$ for a quasiparticle beam of power $\dot{Q} = 23.5 \text{ pW}$. The measurement was made at a temperature $T \approx 120 \text{ }\mu\text{K}$ at 0 bar pressure. The line shows the model calculation given by Eq. 7 assuming that the centre of the beam is offset from the centre pixel by 0.55 mm (Color figure online)

the applied beam power. The direct contribution from the quasiparticle beam Δf_2^{Beam} is approximately proportional to the flux of quasiparticles in the beam. For an ideal radiator, having a thermal distribution of quasiparticles and a point-like thin orifice, the excitation flux in the beam is

$$\langle n v_g \rangle = \frac{\dot{Q}}{\langle E \rangle} \frac{\cos \theta}{\pi r^2} \tag{5}$$

where r is the distance from the orifice, θ is the angle to the normal of the orifice and $\langle E \rangle = \Delta + kT$ is the mean excitation energy in the beam where T is the temperature inside the radiator. The beam power \dot{Q} is the sum of the applied power and the heat-leak into the radiator.

The face of each pixel has an open area $A_p = \pi R^2$ where $R = 0.5$ mm is the radius of the pixel cavity. The area perpendicular to the local beam direction is approximately $A_p \cos \theta_p$ where θ_p is the angle between the normal of the orifice and the line joining the centre of the face of the pixel to the centre of the orifice. The number of excitations incident on the face of the pixel per unit time is thus

$$\dot{N}_p \approx \frac{\dot{Q}}{\langle E \rangle} A_p \frac{\cos^2 \theta_p}{\pi r_p^2} \tag{6}$$

where r_p is the distance from the centre of the face of the pixel to the centre of the orifice. If we assume that this produces a proportionate increase in damping Δf_2^{Beam} due to the beam then the total quasiparticle damping in each pixel p should be given by

$$\Delta f_{2,p}^{QP} = \Delta f_2^{T0} + B \frac{\cos^2 \theta_p}{\pi r_p^2} \tag{7}$$

where Δf_2^{T0} and B are taken to be fitting parameters.

The line in Fig. 6 shows the expected beam profile based on Eq. 7 assuming that the centre of the beam is offset horizontally from the central pixel by 0.55 mm. It appears that the black-body radiator orifice is centred in between pixels $p = 2$ and $p = 3$. Given the difficulty of aligning the detector within the experimental cell, we are pleased that the offset is relatively small.

The above arguments are expected to overestimate the response for pixels close to the centre of the beam ($p = 2$ and $p = 3$) since for these pixels the incident excitations are not so well thermalised within the pixel. Indeed, we estimate that ~ 10 % of the incident excitations pass straight through the cavities of these pixels without scattering at all. Since the prong motion is almost perpendicular to the beam for these pixels, the lack of thermalisation will result in a lower damping. This is consistent with the data in Fig. 6. Thermalisation could be improved in a future design by making the rear of the pixel cavities closed. However, this would make the design more challenging and it would degrade the thermal performance since the pixels would then re-radiate all of the incident excitations back towards the black-body radiator, whereas in the current design many of the excitations leave from the rear of the pixels towards the surrounding refrigerant sinter stack.

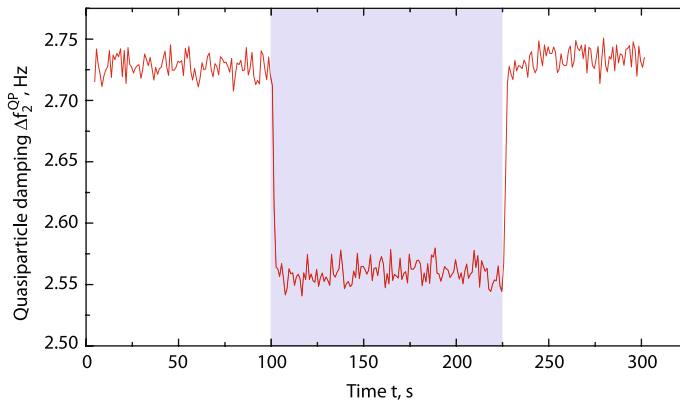


Fig. 7 The quasiparticle shadow cast on the central pixel by vortices created by the generator wire. The pixel is illuminated by a quasiparticle beam of power 716 pW. The quasiparticle damping of the fork in the central pixel ($p = 3$) is shown versus time. In the shaded region the generator is driven to a velocity of 9.8 mm s^{-1} for a period of 125 s. The resulting vortices cast a quasiparticle shadow on the pixel which results in a reduction in the damping. The measurement was made at a temperature $T \approx 170 \text{ } \mu\text{K}$ at 0 bar pressure (Color figure online)

Figure 7 shows a measurement of the quasiparticle shadow cast by vortices on the central pixel, $p = 3$. The pixel is illuminated by a quasiparticle beam of power 716 pW. The quasiparticle damping of the fork in the central pixel ($p = 3$) is shown versus time whilst the generator is driven to a velocity of 9.8 mm s^{-1} for a period of 125 s. The resulting vortices cast a quasiparticle shadow on the pixel which results in a reduction in the damping. The fractional reduction in damping is comparable to that observed in other types of measurements using vibrating wires [36,37,43,44].

7 Summary and Discussion

We have developed a 2-dimensional detector to form a rudimentary quasiparticle camera to image quantum turbulence in superfluid $^3\text{He-B}$ in the low temperature limit. The detector has 25 pixels formed by miniature quartz tuning forks in cylindrical cavities in a copper matrix. The detector is illuminated by a beam of quasiparticle excitations produced by a black-body radiator. Vortices are generated in the path of the beam using a vibrating wire resonator. The vortices Andreev reflect excitations and thus cast a quasiparticle shadow on the detector causing a reduction in damping on the tuning forks. We have described the design and construction of the detector and we have shown preliminary measurements on one row of pixels which demonstrate that the detector is able to measure quasiparticle beams and shadows with good sensitivity. Further experiments will be made to measure the spatial and temporal profile of the vortices and quantum turbulence generated by the nearby wire.

The temporal resolution of the detector is limited by the mechanical time constant of each of the tuning forks, $\tau = 1/(\pi \Delta f_2)$. The time constant of the measuring equipment can be adjusted to suit. The damping from quasiparticle excitations Δf_2^{QP} falls exponentially with decreasing temperature [31] so the time constants become very

long at the lowest temperatures, limited by the the intrinsic damping of the tuning forks. Under typical experimental conditions for observing vortices, such as for the data in Fig. 7, the mechanical time constants are around 0.1 s. This is sufficient to resolve the dominant fluctuations in quantum turbulence which occur on timescales of order 1 s or more [44].

The spatial resolution is approximately 1 mm, limited by the pixel size. This should be sufficient to gain useful information on the spatial profile of vortices generated by the wire as well as their dynamics. Calculations of Andreev reflection from vortices [37] show that under typical experimental conditions a single vortex in a quasiparticle beam will reflect around 2 % of the excitations over a distance of 0.5 mm either side of the core. Currently our measurement noise level is around 1 % so this is already sufficient to observe single vortex lines.

Finally we note that the technique could also be used to image other superfluid structures which scatter excitations. These include orbital textures in the distorted B-phase in high magnetic field [42], textural defects such as boojums [45] and the A-B phase interface [46].

Acknowledgments We thank Statek Corporation for manufacturing the custom-made tuning fork wafers. We thank A. Stokes and M.G. Ward for excellent technical support and P. Skyba for useful discussions. This research was supported by the UK EPSRC and by the European FP7 Programme MICROKELVIN Project, no. 228464.

Open Access This article is distributed under the terms of the Creative Commons Attribution License which permits any use, distribution, and reproduction in any medium, provided the original author(s) and the source are credited.

References

1. M. Blažková, M. Človečko, V.B. Eltsov, E. Gažo, R. de Graaf, J.J. Hosio, M. Krusius, D. Schmoranzer, W. Schoepe, L. Skrbek, P. Skyba, R.E. Soltsev, W.F. Vinen, *J. Low Temp. Phys.* **150**(3–4), 525 (2008). doi:[10.1007/s10909-007-9587-3](https://doi.org/10.1007/s10909-007-9587-3)
2. S.L. Ahlstrom, D.I. Bradley, M. Človečko, S.N. Fisher, A.M. Guénault, E.A. Guise, R.P. Haley, O. Kolosov, M. Kumar, P.V.E. McClintock, G.R. Pickett, E. Polturak, M. Poole, I. Todoshchenko, V. Tsepelin, A.J. Woods, *J. Low Temp. Phys.* **175**, 140 (2014). doi:[10.1007/s10909-013-0930-6](https://doi.org/10.1007/s10909-013-0930-6)
3. D.I. Bradley, P. Crookston, M.J. Fear, S.N. Fisher, G. Foulds, D. Garg, A.M. Guénault, E. Guise, R.P. Haley, O. Kolosov, G.R. Pickett, R. Schanen, V. Tsepelin, *J. Low. Temp. Phys.* **161**(5–6, SI), 536 (2010). doi:[10.1007/s10909-010-0227-y](https://doi.org/10.1007/s10909-010-0227-y)
4. S.L. Ahlstrom, D.I. Bradley, M. Človečko, S.N. Fisher, A.M. Guénault, E.A. Guise, R.P. Haley, O. Kolosov, P.V.E. McClintock, G.R. Pickett, M. Poole, V. Tsepelin, A.J. Woods, *Phys. Rev. B* **85**, 014515 (2014)
5. D.O. Clubb, O.V.L. Buu, R.M. Bowley, R. Nyman, J.R. Owers-Bradley, *J. Low Temp. Phys.* **136**(1/2), 1 (2004)
6. R. Blaauwgeers, M. Blazkova, M. Človečko, V.B. Eltsov, R. de Graaf, J. Hosio, M. Krusius, D. Schmoranzer, W. Schoepe, L. Skrbek, P. Skyba, R.E. Soltsev, D.E. Zmeev, *J. Low Temp. Phys.* **146**(5/6), 537 (2007). doi:[10.1007/s10909-006-9279-4](https://doi.org/10.1007/s10909-006-9279-4)
7. D.I. Bradley, M. Človečko, S.N. Fisher, D. Garg, A.M. Guénault, E. Guise, R.P. Haley, G.R. Pickett, M. Poole, V. Tsepelin, *J. Low Temp. Phys.* **171**, 750 (2013)
8. M. Blažková, D. Schmoranzer, L. Skrbek, *Phys. Rev. E* **75**(2), 025302 (2007). doi:[10.1103/PhysRevE.75.025302](https://doi.org/10.1103/PhysRevE.75.025302)
9. M. Blažková, D. Schmoranzer, L. Skrbek, W.F. Vinen, *Phys. Rev. B* **79**(5), 054522 (2009). doi:[10.1103/PhysRevB.79.054522](https://doi.org/10.1103/PhysRevB.79.054522)

10. D.I. Bradley, M.J. Fear, S.N. Fisher, A.M. Guénault, R.P. Haley, C.R. Lawson, P.V.E. McClintock, G.R. Pickett, R. Schanen, V. Tsepelin, L.A. Wheatland, J. Low, Temp. Phys. **156**(3/6), 116 (2009). doi:[10.1007/s10909-009-9901-3](https://doi.org/10.1007/s10909-009-9901-3)
11. M. Blažková, T.V. Chagovets, M. Rotter, D. Schmoranzer, L. Skrbek, J. Low Temp. Phys. **150**(3–4), 194 (2008). doi:[10.1007/s10909-007-9533-4](https://doi.org/10.1007/s10909-007-9533-4)
12. P. Skyba, D.I. Bradley, M. Človečko, E. Gazo, J. Low Temp. Phys. **152**(5–6), 147 (2008)
13. D.I. Bradley, P. Crookston, S.N. Fisher, A. Ganshin, A.M. Guénault, R.P. Haley, M.J. Jackson, G.R. Pickett, R. Schanen, V. Tsepelin, J. Low, Temp. Phys. **157**(5–6), 476 (2009)
14. A. Salmela, J. Tuoriniemi, T. Rysti, J. Low Temp. Phys. **162**, 678 (2011). doi:[10.1007/s10909-010-0246-8](https://doi.org/10.1007/s10909-010-0246-8)
15. D.I. Bradley, M. Človečko, S.N. Fisher, D. Garg, E. Guise, R.P. Haley, O. Kolosov, G.R. Pickett, V. Tsepelin, D. Schmoranzer, L. Skrbek, Phys. Rev. B **85**, 014501 (2012). doi:[10.1103/PhysRevB.85.014501](https://doi.org/10.1103/PhysRevB.85.014501)
16. D. Garg, V.B. Efimov, M. Giltrow, P.V.E. McClintock, L. Skrbek, W.F. Vinen, Phys. Rev. B **85**, 144518 (2012). doi:[10.1103/PhysRevB.85.144518](https://doi.org/10.1103/PhysRevB.85.144518)
17. M. Tatsuno, P.W. Bearman, J. Fluid Mech. **211**, 157 (1990). doi:[10.1017/S0022112090001537](https://doi.org/10.1017/S0022112090001537)
18. G.P. Bewley, D.P. Lathrop, K.R. Sreenivasanan, Nature **441**, 588 (2006)
19. G.P. Bewley, K.R. Sreenivasan, D.P. Lathrop, Exp. Fluids **44**, 887 (2008)
20. M.S. Paoletti, M.E. Fisher, K.R. Sreenivasan, D.P. Lathrop, Phys. Rev. Lett. **101**, 154501 (2008)
21. Y.A. Sergeev, C.F. Barenghi, J. Low Temp. Phys. **157**, 429 (2009). doi:[10.1007/s10909-009-9994-8](https://doi.org/10.1007/s10909-009-9994-8)
22. W. Guo, S.B. Cahn, J.A. Nikkel, W.F. Vinen, D.N. McKinsey, Phys. Rev. Lett. **105**, 045301 (2010)
23. A.I. Golov, P.M. Walmsley, P.A. Tompsett, J. Low Temp. Phys. **161**, 509 (2010)
24. D.E. Zmeev, F. Pakpour, P.M. Walmsley, A.I. Golov, W. Guo, D.N. McKinsey, G.G. Ihas, P. McClintock, S.N. Fisher, W.F. Vinen, Phys. Rev. Lett. **110**, 175303 (2013)
25. A.P. Finne, T. Araki, R. Blaauwgeers et al., Nature **424**, 1022 (2003)
26. S.N. Fisher, A.M. Guénault, C.J. Kennedy, G.R. Pickett, Phys. Rev. Lett. **63**, 2566 (1989)
27. S.N. Fisher, G.R. Pickett, R.J. Watts-Tobin, J. Low Temp. Phys. **83**, 225 (1991)
28. N. Suramlshvili, A.W. Baggaley, C.F. Barenghi, Y.A. Sergeev, Phys. Rev. B **85**, 174526 (2012)
29. M.P. Enrico, S.N. Fisher, A.M. Guénault, G.R. Pickett, K. Torizuka, Phys. Rev. Lett. **70**, 1846 (1993)
30. S.N. Fisher, A.M. Guénault, C.J. Kennedy, G.R. Pickett, Phys. Rev. Lett. **69**, 1073 (1992)
31. C. Bäuerle, Yu.M. Bunkov, S.N. Fisher, H. Godfrin, Phys. Rev. B **57**, 14381 (1998)
32. J.J. Hosio, V.B. Eltsov, R. de Graaf, M. Krusius, J. Mäkinen, D. Schmoranzer, Phys. Rev. B **84**, 224501 (2011)
33. D.I. Bradley, S.N. Fisher, A.M. Guénault, M.R. Lowe, G.R. Pickett, A. Rahm, Physica B **329**, 64–65 (2003)
34. D.I. Bradley, S.N. Fisher, A.M. Guénault, M.R. Lowe, G.R. Pickett, A. Rahm, R.C.V. Whitehead, Phys. Rev. Lett. **93**(23), 235302 (2004)
35. D.I. Bradley, S.N. Fisher, A.M. Guénault, R.P. Haley, G.R. Pickett, D. Potts, V. Tsepelin, Nature Phys. **7**, 473 (2011). doi:[10.1038/nphys1963](https://doi.org/10.1038/nphys1963)
36. S.N. Fisher, A.J. Hale, A.M. Guénault, G.R. Pickett, Phys. Rev. Lett. **86**(2), 244 (2001)
37. S.N. Fisher, M.J. Jackson, Y.A. Sergeev, V. Tsepelin, in *Proceedings of the National Academy of Sciences* (2014) (accepted)
38. S. Holt, P. Skyba, Rev. Sci. Instrum. **83**, 064703 (2012). doi:[10.1063/1.4725526](https://doi.org/10.1063/1.4725526)
39. M.P. Enrico, S.N. Fisher, R.J. Watts-Tobin, J. Low Temp. Phys. **98**, 81 (1995)
40. G.R. Pickett, S.N. Fisher, Physica B **75**, 329–333 (2003)
41. D.I. Bradley, S.N. Fisher, A.M. Guénault, R.P. Haley, G.R. Pickett, J. Low Temp. Phys. **135**, 385 (2004)
42. S.N. Fisher, A.M. Guénault, C.J. Kennedy, G.R. Pickett, Phys. Rev. Lett. **67**, 1270 (1991)
43. D.I. Bradley, D.O. Clubb, S.N. Fisher, A.M. Guénault, R.P. Haley, C.J. Matthews, G.R. Pickett, V. Tsepelin, K. Zaki, Phys. Rev. Lett. **95**, 035302 (2005)
44. D.I. Bradley, S.N. Fisher, A.M. Guénault, R.P. Haley, S. O'Sullivan, G.R. Pickett, V. Tsepelin, Phys. Rev. Lett. **101**, 065302 (2008)
45. G.E. Volovik, *Exotic Properties of Superfluid ^3He* (World Scientific, Singapore 1992)
46. D.J. Cousins, M.P. Enrico, S.N. Fisher, S.L. Phillipson, G.R. Pickett, N.S. Shaw, P.J.Y. Thibault, Phys. Rev. Lett. **77**, 5245 (1996)